chiralities (28), which clearly confirms this quantization within the experimental errors. Our measurements demonstrate that even when the global topology has Chern number zero, the distribution of Berry curvature can be very rich.

Our measurement scheme can be readily extended to characterize bands with Chern numbers different from zero (17, 19). In principle, one could start in a shallow lattice, where reaching nonzero Chern numbers is feasible, and for the tomography project onto flat bands, which can be reached, such as by dynamical control over the offset. Our method for generating the topological bands is spin-independent and does not couple different spin states. It therefore can be extended to high-spin systems (29) or to strongly interacting spin mixtures, which are expected to lead to interesting many-body phases (30–32).

REFERENCES AND NOTES

1. M. Z. Hasan, C. L. Kane, *Rev. Mod. Phys.* **82**, 3045–3067 (2010).
2. D. Xiao, M.-C. Chang, Q. Niu, *Rev. Mod. Phys.* **82**, 1959–2007 (2010).
3. M. Hafezi, S. Mittal, J. Fan, A. Migdall, J. M. Taylor, *Nat. Photonics* **7**, 1001–1005 (2013).
4. M. C. Rechtsman *et al.*, *Nature* **496**, 196–200 (2013).
5. Z. Wang, Y. Chong, J. D. Joannopoulos, M. Soljačić, *Nature* **461**, 772–775 (2009).
6. J. Ningyuan, C. Owens, A. Sommer, D. Schuster, J. Simon, *Phys. Rev. X* **5**, 021031 (2015).
7. R. Süsstrunk, S. D. Huber, *Science* **349**, 47–50 (2015).
8. N. Goldman, J. Dalibard, *Phys. Rev. X* **4**, 031027 (2014).
9. T. Kitagawa, E. Berg, M. Rudner, E. Demler, *Phys. Rev. B* **82**, 235114 (2010).
10. T. Oka, H. Aoki, *Phys. Rev. B* **79**, 081406 (2009).
11. E. J. Sie *et al.*, *Nat. Mater.* **14**, 290–294 (2015).
12. M. Bukov, L. D'Alessio, A. Polkovnikov, *Adv. Phys.* **64**, 139–226 (2015).
13. H. Lignier *et al.*, *Phys. Rev. Lett.* **99**, 220403 (2007).
14. J. Struck *et al.*, *Phys. Rev. Lett.* **108**, 225304 (2012).
15. J. Struck *et al.*, *Nat. Phys.* **9**, 738–743 (2013).
16. C. V. Parker, L.-C. Ha, C. Chin, *Nat. Phys.* **9**, 769–774 (2013).
17. G. Jotzu *et al.*, *Nature* **515**, 237–240 (2014).
18. Y.-J. Lin, K. Jiménez-García, I. B. Spielman, *Nature* **471**, 83–86 (2011).
19. M. Aidelsburger *et al.*, *Nat. Phys.* **11**, 162–166 (2015).
20. C. J. Kennedy, W. C. Burton, W. C. Chung, W. Ketterle, *Nat. Phys.* **11**, 859–864 (2015).
21. L. Duca *et al.*, *Science* **347**, 288–292 (2015).
22. T. Li *et al.*, arXiv:1509.02185 (2015).
23. M. Mancini *et al.*, *Science* **349**, 1510–1513 (2015).
24. B. K. Stuhl, H.-I. Lu, L. M. Aycock, D. Genkina, I. B. Spielman, *Science* **349**, 1514–1518 (2015).
25. E. Alba, X. Fernandez-Gonzalvo, J. Mur-Petit, J. K. Pachos, J. J. Garcia-Ripoll, *Phys. Rev. Lett.* **107**, 235301 (2011).
26. P. Hauke, M. Lewenstein, A. Eckardt, *Phys. Rev. Lett.* **113**, 045303 (2014).
27. P. Soltan-Panahi *et al.*, *Nat. Phys.* **7**, 434–440 (2011).
28. Materials and methods are available as supplementary materials on *Science* Online.
29. J. S. Krauser *et al.*, *Science* **343**, 157–160 (2014).
30. T. Neupert, L. Santos, C. Chamon, C. Mudry, *Phys. Rev. Lett.* **106**, 236804 (2011).
31. A. G. Grushin, Á. Gómez-León, T. Neupert, *Phys. Rev. Lett.* **112**, 156801 (2014).
32. N. R. Cooper, J. Dalibard, *Phys. Rev. Lett.* **110**, 185301 (2013).

QUANTUM SIMULATION

Bloch state tomography using Wilson lines

Topology and geometry are essential to our understanding of modern physics, underlying many foundational concepts from high-energy theories, quantum information, and condensed-matter physics. In condensed-matter systems, a wide range of phenomena stem from the geometry of the band eigenstates, which is encoded in the matrix-valued Wilson line for general multiband systems. Using an ultracold gas of rubidium atoms loaded in a honeycomb optical lattice, we realize strong-force dynamics in Bloch bands that are described by Wilson lines and observe an evolution in the band populations that directly reveals the band geometry. Our technique enables a full determination of band eigenstates, Berry curvature, and topological invariants, including single- and multiband Chern and Z_2 numbers.

Tracy Li,[1,2] Lucia Duca,[1,2] Martin Reitter,[1,2] Fabian Grusdt,[3,4,5] Eugene Demler,[5] Manuel Endres,[5,6] Monika Schleier-Smith,[7] Immanuel Bloch,[1,2] Ulrich Schneider[1,2,8]*

Geometric concepts play an increasingly important role in elucidating the behavior of condensed-matter systems. In band structures without degeneracies, the geometric phase acquired by a quantum state during adiabatic evolution elegantly describes a spectrum of phenomena (1). This geometric phase— known as the Berry phase— is used to formulate the Chern number (2), which is the topological invariant characterizing the integer quantum Hall effect (3). However, condensed-matter properties that are determined by multiple bands with degeneracies, such as in topological insulators (4, 5) and graphene (6), can seldom be understood with standard Berry phases. Recent work has shown that such systems can instead be described using Wilson lines (7–10).

Wilson lines encode the geometry of degenerate states (11), providing indispensable information for the ongoing effort to identify the topological structure of bands. For example, the eigenvalues of Wilson-Zak loops (i.e., Wilson lines closed by a reciprocal lattice vector) can be used to formulate the Z_2 invariant of topological insulators (7) and identify topological orders protected by lattice symmetries (8, 9). Although experiments have accessed the geometry of isolated bands through various methods, including transport measurements (3, 12, 13), interferometry (14, 15), and angle-resolved photoemission spectroscopy (5, 16), Wilson lines have thus far remained a theoretical construct (7–10).

Using ultracold atoms in a graphene-like honeycomb lattice, we demonstrate that Wilson lines can be accessed and used as versatile probes of band structure geometry. Whereas the Berry phase merely multiplies a state by a phase factor, the Wilson line is a matrix-valued operator that can mix state populations (11) (Fig. 1A). We measure the Wilson line by detecting changes in the band populations (17) under the influence of an external force, which transports atoms through reciprocal space (18). In the presence of a force $\mathbf{F}$, atoms with initial quasimomentum $\mathbf{q}(0)$ evolve to quasimomentum $\mathbf{q}(t) = \mathbf{q}(0) + \mathbf{F}t/\hbar$ after a time t. If the force is sufficiently weak and the bands are nondegenerate, the system will undergo adiabatic Bloch oscillations and remain in the lowest band (18). In this case, the quantum state merely acquires a phase factor composed of the geometric Berry phase and a dynamical phase. At stronger forces, however, transitions to other bands occur, and the state evolves into a superposition over several bands.

When the force is infinite with respect to a chosen set of bands, the effect of the dispersion vanishes, and the bands appear as effectively degenerate (Fig. 1B). The system then evolves according to the formalism of Wilczek and Zee for adiabatic motion in a degenerate system (11). The unitary time-evolution operator describing the dynamics is the Wilson line matrix (19)

$$\hat{\mathbf{W}}_{\mathbf{q}(0)\to\mathbf{q}(t)} = \mathcal{P}\exp[i\int_{\mathcal{C}} d\mathbf{q}\,\hat{\mathbf{A}}_{\mathbf{q}}] \qquad (1)$$

where the path-ordered ($\mathcal{P}$) integral runs over the path $\mathcal{C}$ in reciprocal space from $\mathbf{q}(0)$ to $\mathbf{q}(t)$ and $\hat{\mathbf{A}}_{\mathbf{q}}$ is the Wilczek-Zee connection, which encodes the local geometric properties of the state space.

In a lattice system with Bloch states $|\Phi_{\mathbf{q}}^n\rangle = e^{i\mathbf{q}\cdot\hat{\mathbf{r}}}|u_{\mathbf{q}}^n\rangle$ in the nth band at quasimomentum $\mathbf{q}$, where $\hat{\mathbf{r}}$ is the position operator, the elements of the Wilczek-Zee connection are determined by the cell-periodic part $|u_{\mathbf{q}}^n\rangle$ as $\mathbf{A}_{\mathbf{q}}^{n,n'} = i\langle u_{\mathbf{q}}^n|\nabla_{\mathbf{q}}|u_{\mathbf{q}}^{n'}\rangle$. The diagonal elements ($n = n'$) are the Berry connections of the individual Bloch bands, which yield the Berry phase when integrated along a

[1]Fakultät für Physik, Ludwig-Maximilians-Universität München, Schellingstrasse 4, 80799 Munich, Germany. [2]Max-Planck-Institut für Quantenoptik, Hans-Kopfermann-Str. 1, 85748 Garching, Germany. [3]Department of Physics and Research Center OPTIMAS, University of Kaiserslautern, Germany. [4]Graduate School Materials Science in Mainz, Gottlieb-Daimler-Strasse 47, 67663 Kaiserslautern, Germany. [5]Department of Physics, Harvard University, Cambridge, MA 02138, USA. [6]Institute for Quantum Information and Matter, Department of Physics, California Institute of Technology, Pasadena, CA 91125, USA. [7]Department of Physics, Stanford University, Stanford, CA 94305, USA. [8]Cavendish Laboratory, University of Cambridge, J. J. Thomson Avenue, Cambridge CB3 0HE, UK.
*Corresponding author. Email: uws20@cam.ac.uk

closed path. The off-diagonal elements ($n \neq n'$) are the interband Berry connections, which couple the bands and induce interband transitions.

Although the evolution described by Eq. 1 must be path-ordered when the Wilczek-Zee connections at different quasimomenta do not commute, it can also be path-independent under certain circumstances (9, 20). For example, when the relevant bands span the same Hilbert space for all quasimomenta, as is the case in our system, the Wilson line operator describing transport of a Bloch state from $\mathbf{Q}$ to $\mathbf{q}$ reduces to $\tilde{\mathbf{W}}_{\mathbf{Q} \to \mathbf{q}} = e^{i(\mathbf{q}-\mathbf{Q})\cdot\hat{\mathbf{r}}}$ (9, 19, 21)). Consequently, the elements of the Wilson line operator simply measure the overlap between the cell-periodic Bloch functions at the initial and final quasimomenta (9, 21)

$$W_{\mathbf{Q} \to \mathbf{q}}^{mn} = \langle \Phi_{\mathbf{q}}^m | e^{i(\mathbf{q}-\mathbf{Q})\cdot\hat{\mathbf{r}}} | \Phi_{\mathbf{Q}}^n \rangle = \langle u_{\mathbf{q}}^m | u_{\mathbf{Q}}^n \rangle \quad (2)$$

Hence, access to the Wilson line elements facilitates the characterization of band structure topology in both path-dependent and path-independent evolution. In both cases, the topological information

is encoded in the eigenvalues of the Wilson-Zak loops. In the latter case, the simplified form of the Wilson line in Eq. 2 additionally enables a map of the cell-periodic Bloch functions over the entire Brillouin zone (BZ) in the basis of the states $|u_{\mathbf{Q}}^n\rangle$ at the initial quasimomentum $\mathbf{Q}$.

We create the honeycomb lattice by interfering three blue-detuned laser beams at 120(1)° angles (Fig. 2A). At a lattice depth $V_0 = 5.2(1)E_r$, where $E_r = h^2/(2m\lambda_L^2)$ is the recoil energy, λ_L is the laser wavelength, and m is the mass of ^{87}Rb, the combined width $\varepsilon \approx h \times 3$ kHz of the lowest two bands is much smaller than the $h \times 15$ kHz gap to higher bands. Consequently, there exists a regime of forces where transitions to higher bands are suppressed, and the system is well approximated by a two-band model (19).

We probe the lattice geometry with a nearly pure Bose-Einstein condensate of ^{87}Rb, which is initially loaded into the lowest band at quasimomentum $\mathbf{q} = \Gamma$, the center of the BZ (Fig. 2B). To move the atoms in reciprocal space, we linearly sweep the frequency of the beams to uniformly accelerate the lattice, thereby generating a constant inertial

force in the lattice frame. By independently controlling the frequency sweep rate of two beams (Fig. 2A), we can tune the magnitude and direction of the force and move the atoms along arbitrary paths in reciprocal space.

To verify that we can access the Wilson line regime, where the dynamics are governed entirely by geometric effects, we transport the atoms from Γ to different final quasimomenta using a variable force $|\mathbf{F}|$ and perform band-mapping (17) to measure the population remaining in the lowest band (Fig. 2C). For vanishing forces, we recover the adiabatic limit, where the population remains in the lowest band. For increasing forces (i and ii in Fig. 1B), where the gradient $|\mathbf{F}|d$ over the distance between A and B sites d is less than the combined width ε, the population continuously decreases. However, at strong forces (iii in Fig. 1B), where $|\mathbf{F}|d > \varepsilon$, the population saturates at a finite value. For example, after transport by one reciprocal lattice vector (blue data in Fig. 2C), about one-quarter of the atoms remain in the first band, in stark contrast to typical Landau-Zener dynamics, where the population vanishes for strong forces (22).
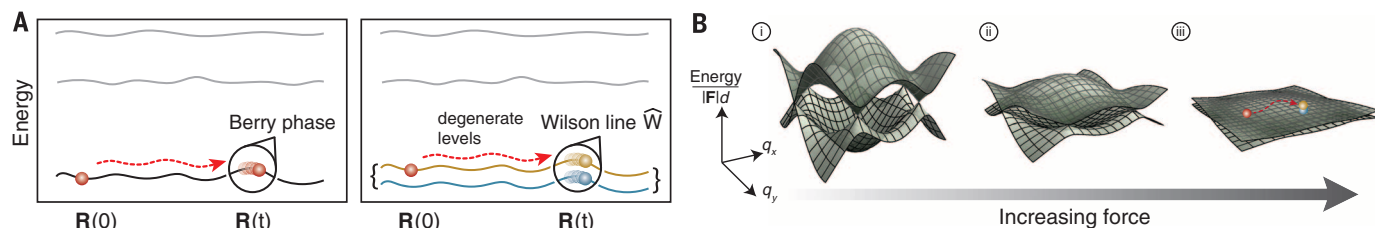

Fig. 1. Wilson lines and effectively degenerate Bloch bands. (**A**) In a nondegenerate system (left), adiabatic evolution of a state through parameter space $\mathbf{R}$ results in the acquisition of a geometric phase factor, known as the Berry phase. In a degenerate system (right), the evolution is instead governed by a matrix-valued quantity called the Wilson line. If the degenerate levels can be experimentally distinguished (blue and yellow coloring), then population changes between the levels are detectable. (**B**) The band structure of the lowest two bands of the honeycomb lattice is given in effective energy units of $|\mathbf{F}|d$, where $\mathbf{F}$ is the applied force used to transport the atoms and d is the distance between nearest-neighbor lattice sites. As $|\mathbf{F}|$ is increased, the largest energy scale of the bands becomes small compared to $|\mathbf{F}|d$. At large forces (iii), the effect of the band energies is negligible, and the system is effectively degenerate. In this regime, the evolution is governed by the Wilson line operator. We distinguish between the bands using a band-mapping technique that detects changes in the band population along the Wilson line path.
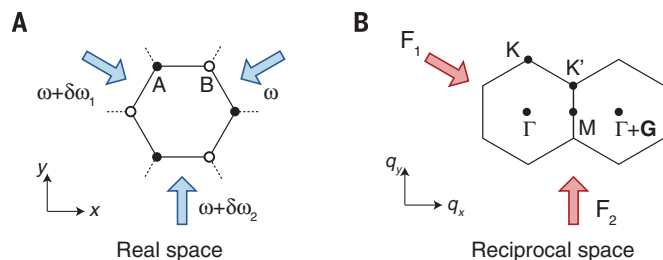
Fig. 2. Reaching the Wilson line regime in the honeycomb lattice. (**A**) Schematic of the honeycomb lattice in real space with A (B) sublattice sites denoted by solid (open) circles. The lattice is formed by interfering three in-plane laser beams (blue arrows) with frequency ω. Sweeping the frequency of beam i by δω$_i$ creates a force $\mathbf{F}_i$ in the lattice frame in the propagation direction of beam i (19). (**B**) Two copies of the first BZ of the honeycomb lattice, separated by a reciprocal lattice vector $\mathbf{G}$. By changing the relative strengths of $\mathbf{F}_i$ (red arrows), the atoms can be moved along arbitrary paths in reciprocal space. Each BZ features nonequivalent Dirac points K and K' at the corners of the hexagonal cell. High-symmetry points Γ, at the center of the BZ, and M, at the edge of the BZ, are also shown. (**C**) The population remaining in the first band for different forces after transport to $\Gamma + 0.2\mathbf{G}$ (green), $\Gamma + 0.55\mathbf{G}$ (red), and $\Gamma + \mathbf{G}$ (blue). Inset numbers i to iii refer to band schematics in Fig. 1B, representing the diminishing
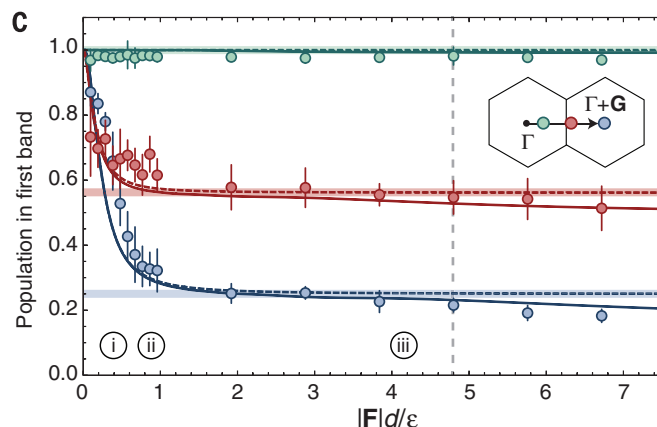
effect of the dispersion for increasing force. The data agree well with a two-level, tight-binding model (dashed line) that approaches the Wilson line regime (thick shaded line) at large forces. Discrepancies at larger forces result from transfer to higher bands and match well with ab initio theory using a full band structure calculation including the first six bands (thin solid line) (19). For all subsequent data, we use $|\mathbf{F}|d/\varepsilon = 4.8$, indicated by the dashed gray line. Error bars indicate the standard error of the mean (SEM) from 10 shots per data point.
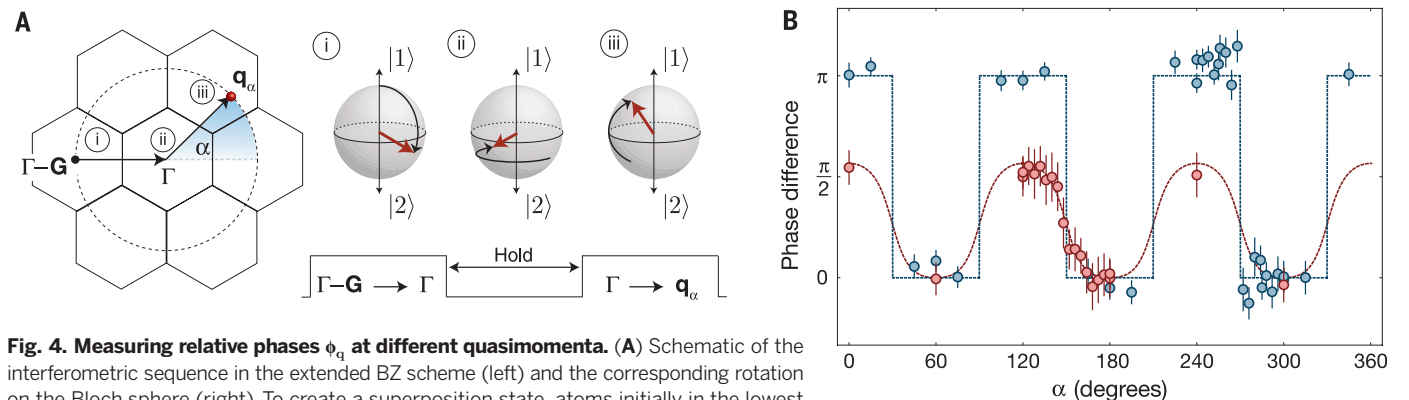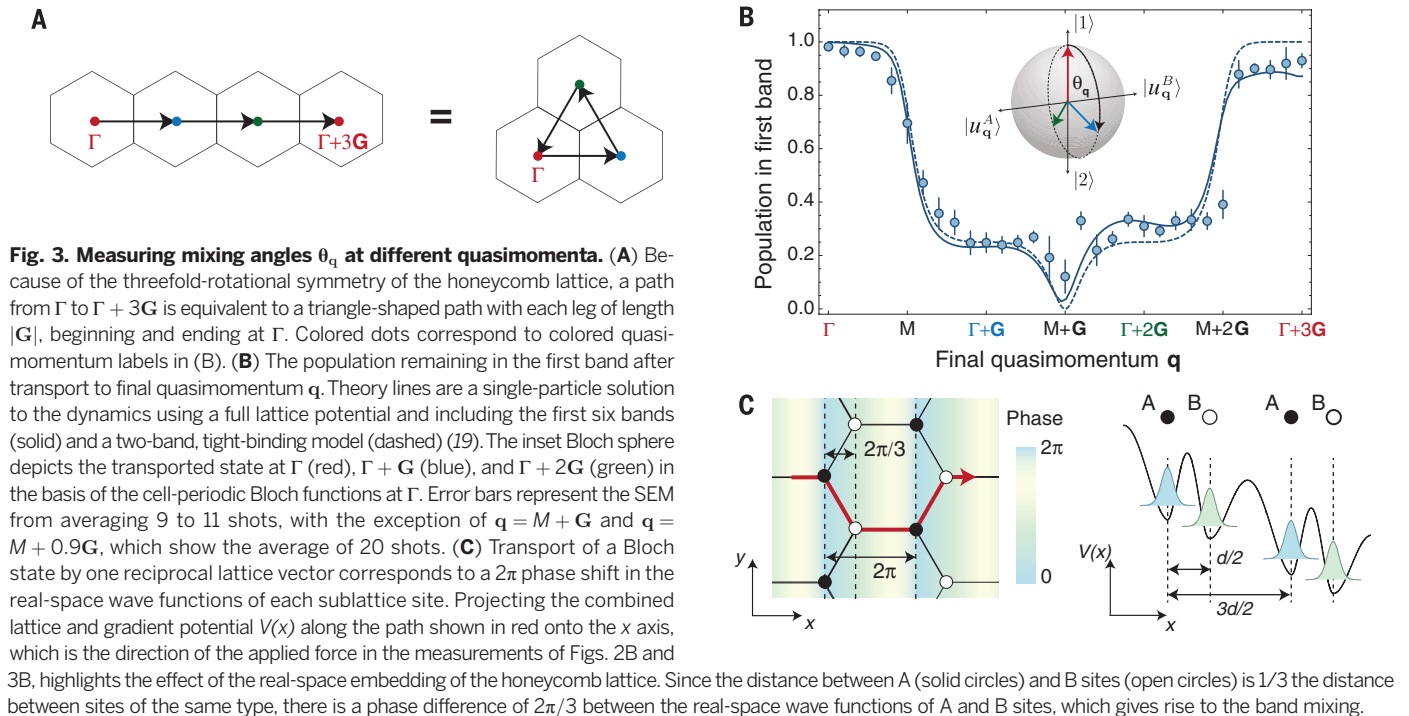
Theoretically, the population in the first band after the strong-force transport directly measures the Wilson line element $|W_{\Gamma \to q}^{11}|^2 = |\langle \Phi_q^1 | \hat{W}_{\Gamma \to q} | \Phi_\Gamma^1 \rangle|^2$ in the basis of the band eigenstates. Based on Eq. 2, the saturation value $|W_{\Gamma \to q}^{11}|^2 = |\langle u_q^1 | u_\Gamma^1 \rangle|^2$ of the population after transport to q is a measure of the overlap between the cell-periodic Bloch functions of the first band $|u_q^1\rangle$ at Γ and q. Notably, for the case of transport by one reciprocal lattice vector G, the cell-periodic parts $|u_q^n\rangle$ are not identical, despite the unity overlap of the Bloch states $|\Phi_q^n\rangle$ at Γ and $\Gamma + G$. In contrast to the typical Landau-Zener case, they are also not orthogonal—hence the finite saturation value.

To corroborate that our experiment measures the Wilson line, we transport atoms initially in

the ground state at Γ by up to three reciprocal lattice vectors (Fig. 3). The threefold rotational symmetry of the lattice, combined with the symmetry of its s-orbitals, makes the path from Γ to $\Gamma + 3G$ equivalent to the triangular path shown in Fig. 3A, such that the overlap between cell-periodic components of the Bloch wave functions at the two endpoints is unity (see Eq. 2). Correspondingly, we expect to recover all the population in the lowest band after transport from Γ to $\Gamma + 3G$. This prediction is confirmed in Fig. 3B, where we plot the population remaining in the first band after transport to final quasimomentum q. The data are well described by a tight-binding model that takes into account the relative phase between orbitals on A and B sites of the lattice due to the Wilson line $\hat{W}_{\Gamma \to q} = e^{iq\cdot\hat{r}}$. Physically,

this can be understood by assuming that the real-space wave function simply accumulates a position-dependent phase when the strong force $F = \hbar(q - Q)/t$ is applied for a short time t (Fig. 3C). Notably, the result depends crucially on the real-space embedding of the lattice and would be different in, e.g., a brick-wall incarnation (23) of the same tight-binding model. Discrepancies from the tight-binding model result from population transfer to higher bands (19).

As the Wilson line enables a comparison of the cell-periodic Bloch functions at any two quasimomenta (Eq. 2), it can in principle be applied to fully reconstruct these states throughout reciprocal space. To this end, it is convenient to represent the state $|u_q^1\rangle$ at quasimomentum q in the basis of cell-periodic Bloch functions

Fig. 3. Measuring mixing angles θ_q at different quasimomenta. (**A**) Because of the threefold-rotational symmetry of the honeycomb lattice, a path from Γ to $\Gamma + 3G$ is equivalent to a triangle-shaped path with each leg of length $|G|$, beginning and ending at Γ. Colored dots correspond to colored quasi-momentum labels in (B). (**B**) The population remaining in the first band after transport to final quasimomentum q. Theory lines are a single-particle solution to the dynamics using a full lattice potential and including the first six bands (solid) and a two-band, tight-binding model (dashed) (19). The inset Bloch sphere depicts the transported state at Γ (red), $\Gamma + G$ (blue), and $\Gamma + 2G$ (green) in the basis of the cell-periodic Bloch functions at Γ. Error bars represent the SEM from averaging 9 to 11 shots, with the exception of $q = M + G$ and $q = M + 0.9G$, which show the average of 20 shots. (**C**) Transport of a Bloch state by one reciprocal lattice vector corresponds to a 2π phase shift in the real-space wave functions of each sublattice site. Projecting the combined lattice and gradient potential $V(x)$ along the path shown in red onto the x axis, which is the direction of the applied force in the measurements of Figs. 2B and 3B, highlights the effect of the real-space embedding of the honeycomb lattice. Since the distance between A (solid circles) and B sites (open circles) is 1/3 the distance between sites of the same type, there is a phase difference of $2\pi/3$ between the real-space wave functions of A and B sites, which gives rise to the band mixing.

Fig. 4. Measuring relative phases ϕ_q at different quasimomenta. (**A**) Schematic of the interferometric sequence in the extended BZ scheme (left) and the corresponding rotation on the Bloch sphere (right). To create a superposition state, atoms initially in the lowest eigenstate at $\Gamma - G$ are rapidly transported to Γ (i). The phase of the superposition state is controlled by varying the hold time at Γ (ii). After the state preparation, the atoms are transported to a final quasimomentum q_α, which is parametrized by the angle α and lies on a circle of radius $|G|$ centered at Γ (iii). (**B**) Phases ϕ_α referenced to $\alpha = 180°$ for the lattice with AB-site degeneracy (blue) and AB-site offset (red). Data in blue have been offset by +120° for visual clarity. Dashed lines are a two-band, tight-binding calculation with $\Delta/J = 0$ (blue) and $\Delta/J = 3.1$ (red), where $J = h \times 500(10)$ Hz. Error bars indicate fit errors.

$|1\rangle = |u_{\mathbf{Q}}^1\rangle$ and $|2\rangle = |u_{\mathbf{Q}}^2\rangle$ at a fixed reference quasimomentum $\mathbf{Q}$ as

$$|u_{\mathbf{q}}^1\rangle = \cos\frac{\theta_{\mathbf{q}}}{2}|1\rangle + \sin\frac{\theta_{\mathbf{q}}}{2}e^{i\phi_{\mathbf{q}}}|2\rangle \qquad (3)$$

Mapping out the geometric structure of the lowest band therefore amounts to obtaining $\theta_{\mathbf{q}}$ and $\phi_{\mathbf{q}}$, which parametrize the amplitude and phase of the superposition between the reference Bloch states, for each quasimomentum $\mathbf{q}$ (24, 25). Whereas the total phase of $|u_{\mathbf{q}}^1\rangle$ is gauge dependent—i.e., it can be chosen for each $\mathbf{q}$—the relative phase $\phi_{\mathbf{q}}$ is fixed for all $\mathbf{q}$ once the basis states $|1\rangle$ and $|2\rangle$ are fixed. Throughout this work, we choose the basis states at reference point $\mathbf{Q} = \Gamma$.

In this framework, the population measurements in Fig. 3B constitute a reconstruction of the mixing angle $\theta_{\mathbf{q}} = 2\arccos|W_{\Gamma\to\mathbf{q}}^{11}|$. This can be visualized as the rotation of a pseudospin on a Bloch sphere, where the north (south) pole represents $|1\rangle$ ($|2\rangle$). As a function of quasimomentum $\mathbf{q}$, the angle $\theta_{\mathbf{q}}$ winds by $2\pi/3$ per reciprocal lattice vector (see inset of Fig. 3B).

To obtain the relative phase $\phi_{\mathbf{q}}$, which is directly connected to the Wilson line via $\phi_{\mathbf{q}} = \mathrm{Arg}[W_{\mathbf{Q}\to\mathbf{q}}^{11}] - \mathrm{Arg}[W_{\mathbf{Q}\to\mathbf{q}}^{12}]$ (19), we perform a procedure analogous to Ramsey or Stückelberg interferometry (26, 27). We initialize atoms in the lowest band at $\Gamma - \mathbf{G}$ and rapidly transport them by one reciprocal lattice vector to prepare a superposition of band eigenstates at the reference point Γ (i in Fig. 4A). We then hold the atoms at Γ for a variable time (ii), during which the phase of the superposition state precesses at a frequency set by the energy difference between the bands at Γ. Following this preparation sequence, we rapidly transport the superposition state to a final quasimomentum $\mathbf{q}_\alpha$, lying at angular coordinate α on a circle of radius $|\mathbf{G}|$ centered at Γ. Measuring the population of the first band as a function of hold time yields an interference fringe that reveals the relative phase ϕ_α (19).

We observe quantized jumps of π in the phase of the interference fringe each time α is swept through a Dirac point, i.e., every 60° (blue circles in Fig. 4B) (28, 29). The binary nature of the phases is a consequence of the degeneracy between A and B sites, which dictates that the band eigenstates at each quasimomentum be an equal superposition of states $|\Phi_{\mathbf{q}}^A\rangle$ and $|\Phi_{\mathbf{q}}^B\rangle$ on the A and B sublattices (19). Therefore, on the Bloch sphere, the pseudospin is constrained to rotate on a meridian about an axis whose poles represent the corresponding cell-periodic functions $|u_{\mathbf{q}}^A\rangle$ and $|u_{\mathbf{q}}^B\rangle$ (inset of Fig. 3B). When we remove this constraint by introducing an energy offset between A and B sites (19, 30), we observe smoothly varying phases that are always less than π (red circles in Fig. 4B). The dependence of the phase on angle α indicates both the breaking of inversion symmetry and the preservation of the three-fold rotational symmetry of the lattice.

Apart from reconstructing the cell-periodic Bloch functions, our method also provides access to eigenvalues of Wilson-Zak loops, $\hat{W}_{\mathbf{q}\to\mathbf{q}+\mathbf{G}}$, which is essential for determining various topological invariants (7–9). To this end, we split the Wilson-Zak-loop matrix into a global phase factor, which can be measured by extending previous methods (13–15, 31), and an $SU(2)$ matrix with eigenvalues $e^{\pm i\xi}$. Using the data from Figs. 3B and 4B, we reconstruct the eigenvalues for a loop transporting from Γ to $\Gamma + \mathbf{G}$, up to multiples of π (19). We find the eigenvalue phases to be $\xi = 1.03(2)\pi/3$, in good agreement with the value of $\pi/3$ predicted from the two-band model. Notably, we measure the same eigenvalues even when the band eigenstates are modified by an energy offset between A and B sites (19). This invariance is a direct consequence of the real-space representation of the Wilson-Zak loop, $\hat{W}_{\Gamma\to\Gamma+\mathbf{G}} = e^{i\mathbf{G}\cdot\hat{\mathbf{r}}}$ [see Eq. 2 and (19)]. Because the Wilson-Zak loop depends only on the position operator $\hat{\mathbf{r}}$, the eigenvalues are determined solely by the physical locations of the lattice sites, which are unchanged by the energy offset.

Our versatile approach only employs standard techniques that are broadly applicable in ultracold-atom experiments and can be extended to higher numbers of bands by adopting ideas from quantum process tomography (32). Provided that the relevant local Hilbert space is identical for all quasimomenta, our method provides a complete map of the eigenstates over the BZ, giving access to the Berry curvature and Chern number. When this is not the case, the same techniques enable the reconstruction of Wilson-Zak loop eigenvalues, which directly probe the geometry of the Wannier functions (9) and, therefore, the polarization of the system (21, 33). Consequently, these eigenvalues can reveal the topology of bands with path-dependent and non-Abelian Wilson lines (9, 11). Such systems can be realized in cold-atom experiments by periodically modulating the lattice (12, 30, 34–36) to create a quasimomentum-dependent admixture of additional bands (37) or coupling between internal states (38–41). Moreover, the addition of spin-orbit coupling (42) would enable the investigation of the Z_2 invariant characterizing time-reversal invariant topological insulators (33, 41, 43–46).

REFERENCES AND NOTES

1. D. Xiao, M.-C. Chang, Q. Niu, *Rev. Mod. Phys.* **82**, 1959–2007 (2010).
2. D. J. Thouless, M. Kohmoto, M. P. Nightingale, M. den Nijs, *Phys. Rev. Lett.* **49**, 405–408 (1982).
3. K. Klitzing, G. Dorda, M. Pepper, *Phys. Rev. Lett.* **45**, 494–497 (1980).
4. M. Z. Hasan, C. L. Kane, *Rev. Mod. Phys.* **82**, 3045–3067 (2010).
5. X.-L. Qi, S.-C. Zhang, *Rev. Mod. Phys.* **83**, 1057–1110 (2011).
6. A. H. Castro Neto, F. Guinea, N. M. R. Peres, K. S. Novoselov, A. K. Geim, *Rev. Mod. Phys.* **81**, 109–162 (2009).
7. R. Yu, X. L. Qi, A. Bernevig, Z. Fang, X. Dai, *Phys. Rev. B* **84**, 075119 (2011).
8. A. Alexandradinata, B. A. Bernevig, http://arxiv.org/abs/1409.3236 (2014).
9. A. Alexandradinata, X. Dai, B. Bernevig, *Phys. Rev. B* **89**, 155114 (2014).
10. F. Grusdt, D. Abanin, E. Demler, *Phys. Rev. A* **89**, 043621 (2014).
11. F. Wilczek, A. Zee, *Phys. Rev. Lett.* **52**, 2111–2114 (1984).
12. G. Jotzu et al., *Nature* **515**, 237–240 (2014).
13. M. Aidelsburger et al., *Nat. Phys.* **11**, 162–166 (2014).
14. L. Duca et al., *Science* **347**, 288–292 (2015).
15. M. Atala et al., *Nat. Phys.* **9**, 795–800 (2013).
16. M. Zahid Hasan, S.-Y. Xu, M. Neupane, in *Topological Insulators: Fundamentals and Perspectives* (Wiley-VCH, Weinheim, Germany, 2015), pp. 55–100.
17. M. Greiner, I. Bloch, O. Mandel, T. W. Hänsch, T. Esslinger, *Phys. Rev. Lett.* **87**, 160405 (2001).
18. M. Ben Dahan, E. Peik, J. Reichel, Y. Castin, C. Salomon, *Phys. Rev. Lett.* **76**, 4508–4511 (1996).
19. See supplementary materials on *Science* Online.
20. J. W. Zwanziger, M. Koenig, A. Pines, *Annu. Rev. Phys. Chem.* **41**, 601–646 (1990).
21. R. D. King-Smith, D. Vanderbilt, *Phys. Rev. B Condens. Matter* **47**, 1651–1654 (1993).
22. S. Shevchenko, S. Ashhab, F. Nori, *Phys. Rep.* **492**, 1–30 (2010).
23. L. Tarruell, D. Greif, T. Uehlinger, G. Jotzu, T. Esslinger, *Nature* **483**, 302–305 (2012).
24. P. Hauke, M. Lewenstein, A. Eckardt, *Phys. Rev. Lett.* **113**, 045303 (2014).
25. E. Alba, X. Fernandez-Gonzalvo, J. Mur-Petit, J. K. Pachos, J. J. Garcia-Ripoll, *Phys. Rev. Lett.* **107**, 235301 (2011).
26. A. Zenesini, D. Ciampini, O. Morsch, E. Arimondo, *Phys. Rev. A* **82**, 065601 (2010).
27. S. Kling, T. Salger, C. Grossert, M. Weitz, *Phys. Rev. Lett.* **105**, 215301 (2010).
28. L.-K. Lim, J.-N. Fuchs, G. Montambaux, *Phys. Rev. Lett.* **112**, 155302 (2014).
29. L.-K. Lim, J.-N. Fuchs, G. Montambaux, *Phys. Rev. A* **91**, 042119 (2015).
30. S. K. Baur, M. H. Schleier-Smith, N. R. Cooper, *Phys. Rev. A* **89**, 051606 (2014).
31. D. A. Abanin, T. Kitagawa, I. Bloch, E. Demler, *Phys. Rev. Lett.* **110**, 165304 (2013).
32. J. F. Poyatos, J. I. Cirac, P. Zoller, *Phys. Rev. Lett.* **78**, 390–393 (1997).
33. A. A. Soluyanov, D. Vanderbilt, *Phys. Rev. B* **83**, 035108 (2011).
34. M. Aidelsburger et al., *Phys. Rev. Lett.* **111**, 185301 (2013).
35. H. Miyake, G. A. Siviloglou, C. J. Kennedy, W. C. Burton, W. Ketterle, *Phys. Rev. Lett.* **111**, 185302 (2013).
36. N. H. Lindner, G. Refael, V. Galitski, *Nat. Phys.* **7**, 490–495 (2011).
37. C. V. Parker, L.-C. Ha, C. Chin, *Nat. Phys.* **9**, 769–774 (2013) Letter.
38. Y. J. Lin, R. L. Compton, K. Jiménez-García, J. V. Porto, I. B. Spielman, *Nature* **462**, 628–632 (2009).
39. N. R. Cooper, *Phys. Rev. Lett.* **106**, 175301 (2011).
40. J. Dalibard, F. Gerbier, G. Juzeliūnas, P. Öhberg, *Rev. Mod. Phys.* **83**, 1523–1543 (2011).
41. B. Béri, N. R. Cooper, *Phys. Rev. Lett.* **107**, 145301 (2011).
42. Y.-J. Lin, K. Jiménez-García, I. B. Spielman, *Nature* **471**, 83–86 (2011).
43. N. Goldman et al., *Phys. Rev. Lett.* **105**, 255302 (2010).
44. G. Liu, S.-L. Zhu, S. Jiang, F. Sun, W. M. Liu, *Phys. Rev. A* **82**, 053605 (2010).
45. C. J. Kennedy, G. A. Siviloglou, H. Miyake, W. C. Burton, W. Ketterle, *Phys. Rev. Lett.* **111**, 225301 (2013).
46. F. Mei, S.-L. Zhu, Z.-M. Zhang, C. H. Oh, N. Goldman, *Phys. Rev. A* **85**, 013638 (2012).

Science

Bloch state tomography using Wilson lines

Tracy Li, Lucia Duca, Martin Reitter, Fabian Grusdt, Eugene Demler, Manuel Endres, Monika Schleier-Smith, Immanuel Bloch and Ulrich Schneider

Cold atoms do geometry

Electrons in solids populate energy bands, which can be simulated in cold atom systems using optical lattices. The geometry of the corresponding wave functions determines the topological properties of the system, but getting a direct look is tricky. Fläschner *et al.* and Li *et al.* measured the detailed structure of the band wave functions in hexagonal optical lattices, one resembling a boron-nitride and the other a graphene lattice. These techniques will make it possible to explore more complex situations that include the effects of interactions.
Science, this issue pp. 1091 and 1094

ARTICLE TOOLS	http://science.sciencemag.org/content/352/6289/1094
SUPPLEMENTARY MATERIALS	http://science.sciencemag.org/content/suppl/2016/05/25/352.6289.1094.DC1
RELATED CONTENT	http://science.sciencemag.org/content/sci/352/6289/1091.full
REFERENCES	This article cites 47 articles, 1 of which you can access for free http://science.sciencemag.org/content/352/6289/1094#BIBL
PERMISSIONS	http://www.sciencemag.org/help/reprints-and-permissions

Use of this article is subject to the Terms of Service